

# Statistical Modeling and Simulation of Short-Range Device-to-Device Communication Channels at sub-THz Frequencies

Seunghwan Kim *Student Member, IEEE*, and Alenka Zajić *Senior Member, IEEE*,

**Abstract**—A two-dimensional (2-D) geometrical propagation model for short-range device-to-device desktop communication channels at sub-terahertz (sub-THz) frequencies is proposed. Based on the geometrical model, a parametric reference model for short-range sub-THz multipath fading channels is developed. From the reference model, the corresponding frequency correlation function (FCF) and power delay profile (PDP) are derived and compared with measured data. The results show good agreement between the measured and theoretical PDP's. Finally, a new sum-of-sinusoids based simulation model for wideband sub-THz channels is proposed. The statistics of the reference model are verified by simulation. The results show that the simulation model is a good approximation of the reference model.

**Index Terms**—sub-THz channels, short-range, desktop channels, statistical characterization, channel modeling, channel sounding.

## I. INTRODUCTION

WIRELESS traffic volume is expected to expand tremendously in the next few years and wireless data rates exceeding 10 Gbit/s will be required in the near future [1]. The opening up of carrier frequencies in the terahertz-range (THz) is the most promising approach to provide sufficient bandwidth required for ultra-fast and ultra-broadband data transmissions [2]. A suitable frequency windows can be found around 110 – 170 GHz (D-band), and around 300 – 350 GHz. The large bandwidths paired with higher speed wireless links can open the door to a large number of novel applications such as ultra-high-speed pico-cell cellular links, wireless short-range communications, secure wireless communication for military and defense applications, and on-body communication for health monitoring systems. This paper focuses on short-range communication between devices on a desktop or chip-to-chip communication (IEEE P802.15.3d).

To successfully design short-range device-to-device sub-THz communication systems, it is necessary to have a detailed knowledge of the multipath fading channel and its statistical properties. To understand the propagation in indoor environments, measurements at 300 – 310 GHz [3], [4] have been reported for two indoor scenarios: 1) a free-space link of devices on a desktop and 2) a free-space connection of a

laptop to an access point in the middle of an office. Recently, THz measurements and statistical characterization of 300 GHz channel with a bandwidth of 20 GHz have been reported in [5], [6] for a free-space link of devices on a desktop, the first indoor measurements of 110 – 170 GHz channel have been reported in [7], and first chip-to-chip measurements of 300 – 320 GHz channel have been reported in [8].

The first ray-tracing and path-loss models for THz communications have been reported in [9]-[17]. Furthermore, the first statistical model for THz channels has been reported in [18]. The proposed model adapts the frequency-dependent path gains model [19] and the indoor Saleh-Valenzuela model [20] for THz frequencies by running large number of ray-tracing models to extract statistical parameters needed for the model. While this approach significantly simplifies channel simulations, it does not provide an easy insight into statistics such as a correlation function (i.e. function that characterizes how fast a wireless channel changes with time, movement, or in frequency) and/or a power delay profile (i.e. function that characterizes multipath propagation). These statistics enable the system designer to make informed decisions when choosing modulation, interleaving, and coding schemes at the transmitting end and the type of channel estimator and decoder at the receiving end.

To address this problem, we have proposed the geometry-based statistical channel model for short-range device-to-device sub-THz scatter channels [21]. In the proposed model, we consider point-to-point communication link between two stationary directional antennas. Directional antennas are necessary for sub – THz indoor communications due to high path loss at these frequencies [3], [6], [18]. The high antenna directivity gives rise to a scattering pattern that is somewhat different from other indoor (GHz or mm – wave) channels observed in [22]-[30]. In addition to scattering mechanisms that are common to all indoor channels, in sub-THz channels, signals may reflect off the objects that are behind the receive ( $R_x$ ) antenna, travel back to the objects near the transmit ( $T_x$ ) antenna and reflect back to be received by the  $R_x$  antenna. This essentially produces the second arriving path, even without any scatterers between the  $T_x$  and  $R_x$ . This phenomenon has been observed in two independent measurement campaigns [3], [6] and while these reflections can be suppressed in channel sounding experiments by putting absorbers around the  $T_x$  and  $R_x$ , in practice, channel models and communication systems need to account for them.

In this paper, we first review our geometrical model for

Paper approved by Dr. Lingjia Liu, the Associate Editor for IEEE Transactions on Wireless Communications. Manuscript received July 21, 2015; revised January 24, 2016 and April 18, 2016; accepted June 9, 2016.

Seunghwan Kim and Alenka Zajić are with the School of Electrical and Computer Engineering, Georgia Institute of Technology, Atlanta, GA, 30332 USA e-mail: (skim745@gatech.edu; alenka.zajic@ece.gatech.edu).

short-range device-to-device wideband sub-THz channels that accounts for line-of-sight (LoS), single-reflection (SR) rays, and double-reflection (DR) rays [21]. To describe our 2-D reference model, we first introduce a 2-D “concentric-sectors” geometrical model for wideband THz channels that consists of concentric sectors filled with scatterers around the  $T_x$  and  $R_x$ . Note that although this model might be perceived as similar to our previous channel models for vehicle-to-vehicle channels [31], [32], the geometry of sectors is significantly different from the geometry of cylinders or circles and leads to different model description. While sectors can be expanded to circles, there are no mechanisms proposed in [31], [32] that allow circles/cylinders to collapse into sectors. This model is chosen to include antenna directionality into the model, one of the key features in THz channels. However, note that by selecting model parameters adequately, sectors can be expended into circles, which allows for omnidirectional antenna pattern. From the geometrical model, we derive new parametric reference model that employs the concentric-sectors geometry and constructs the input delay-spread function as a superposition of LoS, SR, and DR rays. From the new reference model, we derive the corresponding frequency correlation function (FCF) and power delay profile (PDP) for a 2-D isotropic scattering environment. Furthermore, we compare the theoretical PDP’s with the measured ones from [6], [7], and [8]. The results show good agreement between the measured and simulated PDP’s. Furthermore, we propose a sum-of-sinusoids based (SoS) simulation model to overcome the assumption of the reference model that there is an infinite number of scatterers at the  $T_x$  and the  $R_x$ . The statistical properties of our simulation model are verified by comparison with the corresponding statistical properties of the reference model. The results show that the simulation model is a good approximation of the reference model.

The remainder of this paper is organized as follows: Section II introduces the 2-D geometrical concentric-sectors model and presents the parametric reference model that employs the geometry to develop the time-invariant transfer function for short-range THz multipath fading channels. Section III derives the FCF and the PDP for a 2-D isotropic scattering environment and provides comparison between the measured and theoretical PDP’s. Section IV details the statistical SoS simulation model. Finally, few concluding remarks are given in Section V.

## II. A REFERENCE MODEL FOR DEVICE-TO-DEVICE WIDEBAND SUB-THZ CHANNELS

The formulation of reference model for short-range sub-THz device-to-device communication link between the stationary  $T_x$  and  $R_x$  is explained in detail in this section. Both the  $T_x$  and  $R_x$  are equipped with directional antennas, which is a requirement for sub-THz channels to compensate for the high path loss. The radio propagation in indoor environments is characterized by 2-D wide sense stationary uncorrelated scattering (WSSUS) with either LoS or NLoS conditions between the  $T_x$  and  $R_x$ .

Figure 1 shows the concentric-sectors model with LoS, SR, and DR rays. Concentric-sectors are chosen to include antenna

directionality and wideband channel characteristics into the model. In Fig. 1,  $A_T$  and  $A_R$  denote the locations of the  $T_x$  and  $R_x$  antennas and their separation distance is denoted by  $D$ . The scatterers are located along the arcs of the sectors centered at either  $A_T$  or  $A_R$ , with the radius  $R_t$  and  $R_r$ , respectively. The lower-bound of the  $R_t$ ,  $R_{t1}$  is set in the far-field region of the  $T_x$  antenna, and the upper-bound,  $R_{t2}$  is set behind the  $R_x$ . Similarly, the lower-bound of the  $R_r$ ,  $R_{r1}$  is set in the far-field region of the  $R_x$  antenna, and the upper-bound,  $R_{r2}$  is set behind the  $T_x$ . It is assumed that  $M$  fixed omnidirectional scatterers occupy an area between the sectors of radii  $R_{t1}$  and  $R_{t2}$ . These  $M$  omni-directional scatterers lie on  $L$  arcs of radii  $R_{t1} \leq R_t^{(l)} \leq R_{t2}$ , where  $1 \leq l \leq L$ . To account for clustering effect, the  $l^{th}$  arc contains  $M^{(l)}$  fixed omnidirectional scatterers, and the  $(l, m)^{th}$  scatterer is denoted by  $S^{(l,m)}$ , where  $1 \leq m \leq M^{(l)}$ . Similarly,  $Q$  scatterers lie on  $P$  arcs of radii  $R_{r1} \leq R_r^{(p)} \leq R_{r2}$ , where  $1 \leq p \leq P$ . The  $p^{th}$  arc contains  $Q^{(p)}$  fixed omni-directional scatterers and the  $(p, q)^{th}$  scatterer is denoted by  $S^{(p,q)}$ , where  $1 \leq q \leq Q^{(p)}$ .

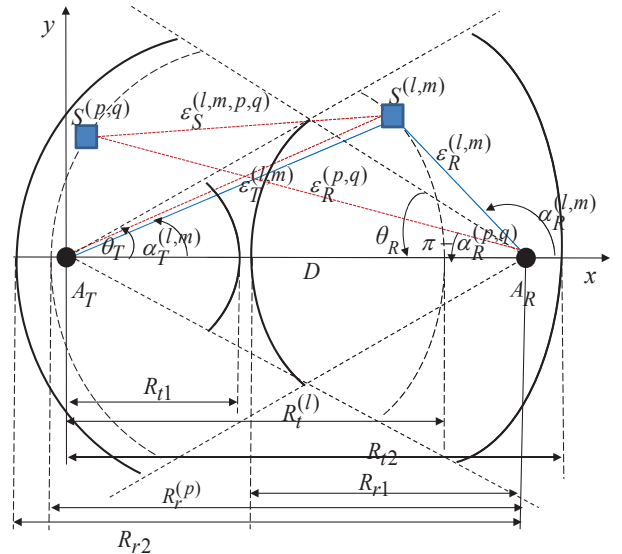


Fig. 1. The concentric-sectors model with LoS, SR, and DR rays for a short-range wideband sub-THz device-to-device channel.

In Fig. 1, the angles  $\theta_T$  and  $\theta_R$  denote the half-beamwidths of the  $T_x$  and  $R_x$  antennas, respectively, relative to the  $x$ -axis. The propagation path lengths  $\epsilon_T^{(l,m)}$ ,  $\epsilon_R^{(l,m)}$ ,  $\epsilon_S^{(l,m,p,q)}$ , and  $\epsilon_R^{(p,q)}$  correspond to the distances  $A_T - S^{(l,m)}$ ,  $S^{(l,m)} - A_R$ ,  $S^{(l,m)} - S^{(p,q)}$ ,  $S^{(p,q)} - A_R$ , respectively, as shown in Fig. 1. Finally, the symbol  $\alpha_T^{(l,m)}$  represents the angle of departure (AoD) of the ray that impinges on the scatterer  $S^{(l,m)}$ , while  $\alpha_R^{(l,m)}$  denotes the angle of arrival (AoA) of the ray that reflects off  $S^{(l,m)}$ . On the other hand, the AoA of the ray that arrives after bouncing off  $S^{(l,m)}$  and  $S^{(p,q)}$ , i.e., double-reflected ray, is denoted by  $\alpha_R^{(p,q)}$ . All the parameters used in the geometrical model are summarized in Table I.

It is observed from the 2-D geometrical model in Fig. 1 that there exist three ray components in the channel: ray that traverses directly from the  $T_x$  to the  $R_x$  antenna (LoS component), ray that impinges upon the scatterers  $S^{(l,m)}$  in the  $R_x$  sector area before arriving at the  $R_x$  antenna (Single-

TABLE I  
DEFINITION OF THE PARAMETERS USED IN THE CONCENTRIC-SECTORS  
GEOMETRICAL MODEL.

$D$	Distance between the centers of Tx and Rx sectors
$R_t^{(l)}$	Radius of the $l$ th sector with its center at Tx.
$R_r^{(p)}$	Radius of the $p$ th sector with its center at Rx.
$\theta_T, \theta_R$	Half-beamwidths of the Tx and Rx antennas in the x-y plane (relative to x-axis), respectively.
$R_{t1}, R_{t2}$	minimum and maximum radii of the sectors with centers at Tx
$R_{r1}, R_{r2}$	minimum and maximum radii of the sectors with centers at Rx
$\alpha_T^{(l,m)}, \alpha_T^{(p,q)}$	Azimuth angles of departure (AAoD) of the waves that impinge on the scatterers $S^{(l,m)}$ and $S^{(p,q)}$ , respectively.
$\alpha_R^{(l,m)}, \alpha_R^{(p,q)}$	Azimuth angles of arrival (AAoA) of the waves scattered from the scatterers $S^{(l,m)}$ and $S^{(p,q)}$ , respectively.
$\epsilon_T^{(l,m)}$	Distance $d(A_T, S^{(l,m)})$
$\epsilon_R^{(l,m)}$	Distance $d(S^{(l,m)}, A_R)$
$\epsilon_S^{(p,q)}$	Distance $d(S^{(p,q)}, A_R)$
$\epsilon_T^{(l,m,p,q)}$	Distance $d(S^{(l,m)}, S^{(p,q)})$
$\epsilon_S$	Distance $d(S^{(l,m)}, S^{(p,q)})$

Reflected component), and/or ray that reflects off the scatterers  $S^{(l,m)}$  in the  $R_x$  sector area and, subsequently, scatters from the scatterers  $S^{(p,q)}$  in the  $T_x$  sector area before arriving at the  $R_x$  antenna (Double-Reflected component). Hence, the time-invariant input delay-spread function of the link  $A_T - A_R$  can be written as a superposition of the LoS, SR, and DR rays, viz.

$$h(t, \tau) = h^{SR}(t, \tau) + h^{DR}(t, \tau) + h^{LoS}(t, \tau). \quad (1)$$

Note that the channel considered in this paper is stationary, and therefore,  $t$  in (1) will be omitted in further equations.

The single-reflected component of the input delay-spread function is

$$h^{SR}(\tau) = \sqrt{\frac{\eta_{SR}}{K+1}} \lim_{M \rightarrow \infty} \frac{1}{\sqrt{M}} \sum_{l=1}^L \sum_{m=1}^{M^{(l)}} A_{l,m} e^{j\phi_{l,m}} \delta(\tau - \tau_{l,m}), \quad (2)$$

where  $A_{l,m}$ ,  $\phi_{l,m}$ , and  $\tau_{l,m}$  are the amplitude, the phase, and the time delay of the multipath components and they are defined as in [21]. Parameter  $K$  is the Rice factor (ratio of LoS to scatter received power).

The double-bounced component of the input delay-spread function is defined as

$$h^{DR}(\tau) = \sqrt{\frac{\eta_{DR}}{K+1}} \lim_{M, Q \rightarrow \infty} \frac{1}{\sqrt{MQ}} \sum_{l,m=1}^{L, M^{(l)}} \sum_{p,q=1}^{P, Q^{(p)}} A_{l,m,p,q} e^{j\phi_{l,m,p,q}} \delta(\tau - \tau_{l,m,p,q}), \quad (3)$$

where  $A_{l,m,p,q}$ ,  $\phi_{l,m,p,q}$ , and  $\tau_{l,m,p,q}$  are the amplitude, the phase, and the time delay of the multipath components and they are defined as in [21]. The parameters,  $\eta_{SR}$  and  $\eta_{DR}$  in (2) and (3), quantify the relative powers allocated to the Single- and Double-Reflected rays, respectively, such that their sum equals 1 (i.e.,  $\eta_{SR} + \eta_{DR} = 1$ ). It is assumed that the angles of departure,  $\alpha_T^{(l,m)}$ , the angles of arrival,  $\alpha_R^{(p,q)}$ , and the radii,  $R_t^{(l)}$  and  $R_r^{(p)}$ , are independent random variables. Furthermore, it is assumed that the phases,  $\phi_{l,m}$ ,  $\phi_{p,q}$ , and  $\phi_{l,m,p,q}$ , are uniform random variables on the interval  $[-\pi, \pi)$  and are independent from the angles of departure, the angles

of arrival, and the radii of the sectors. Note that, for double-reflected rays, the AoA's,  $\alpha_R^{(p,q)}$ , are independent from the AoD's,  $\alpha_T^{(l,m)}$  [33], while single-reflected rays have AoA's,  $\alpha_R^{(l,m)}$ , that are dependent on the AoD's,  $\alpha_T^{(l,m)}$ , and vice versa.

The LoS component of the input delay-spread function is

$$h^{LoS}(\tau) = \sqrt{\frac{K}{K+1}} A_{LoS} e^{j\phi_{LoS}} \delta(\tau - \tau_{LoS}), \quad (4)$$

where the LoS amplitude,  $A_{LoS}$ , and the LoS time delay,  $\tau_{LoS}$ , are defined as in [21].

Finally, we observe that the distances  $\epsilon_T^{(l,m)}$ ,  $\epsilon_R^{(l,m)}$ ,  $\epsilon_S^{(l,m,p,q)}$ , and  $\epsilon_R^{(p,q)}$  can be expressed as functions of the random variables  $\alpha_T^{(l,m)}$ ,  $\alpha_R^{(p,q)}$ ,  $R_t^{(l)}$ , and  $R_r^{(p)}$  as follows:

$$\epsilon_T^{(l,m)} = R_t^{(l)} \quad (5)$$

$$\epsilon_R^{(l,m)} = \frac{R_t^{(l)} \cos \alpha_T^{(l,m)} - D}{\cos \left[ \tan^{-1} \left( -\frac{R_t^{(l)} \sin \alpha_T^{(l,m)}}{D - R_t^{(l)} \cos \alpha_T^{(l,m)}} \right) + \pi \right]} \quad (6)$$

$$\epsilon_S^{(l,m,p,q)} = \left[ \left| R_t^{(l)} \sin \alpha_T^{(l,m)} - R_r^{(p)} \sin \alpha_R^{(p,q)} \right|^2 + \left| R_t^{(l)} \cos \alpha_T^{(l,m)} - R_r^{(p)} \cos \alpha_R^{(p,q)} - D \right|^2 \right]^{1/2} \quad (7)$$

$$\epsilon_R^{(p,q)} = R_r^{(p)}. \quad (8)$$

The derivations of (6) and (7) are presented in Appendix A.

Since the locations of scatterers within an antenna radiation sector are equally probable, we assume uniformly distributed scattering in the concentric-sectors model and to characterize it we use the joint probability density function (pdf)

$$f(R, \alpha) = \frac{2R}{(\alpha_2 - \alpha_1)(R_2^2 - R_1^2)}. \quad (9)$$

The radii,  $R_t^{(l)}$  and  $R_r^{(p)}$ , are uniformly distributed between  $R_{t1}$  and  $R_{t2}$ , and  $R_{r1}$  and  $R_{r2}$ , respectively. Similarly, the AoDs,  $\alpha_T^{(l,m)}$ , and the AoAs,  $\alpha_R^{(p,q)}$ , are uniformly distributed between  $(2\pi - \theta_T) - \theta_T$  and  $(\pi - \theta_R) - (\pi + \theta_R)$ , respectively. Such a distribution implies that the scatterers in the horizontal plane will have a uniform density between the concentric-sectors, if the scattering is isotropic in the horizontal plane.

To simplify further analysis, we use the time-invariant transfer function instead of the input delay-spread function and we normalize the gain patterns of the antenna elements to unity, although other gain patterns can be accommodated at this point. The time-invariant transfer function is the Fourier transform of the input delay-spread function [33] and can be written as

$$T(f) = \mathcal{F}_\tau \{h(\tau)\} = T^{SB}(f) + T^{DB}(f) + T^{LoS}(f), \quad (10)$$

where  $T^{SB}(f)$  is the SB,  $T^{DB}(f)$  is the DB, and  $T^{LoS}(f)$  is the LoS component of the time-invariant transfer function. The expressions for  $T^{SB}(f)$ ,  $T^{DB}(f)$ , and  $T^{LoS}(f)$  are derived in Appendix B.

### III. FREQUENCY CORRELATION FUNCTION AND POWER DELAY PROFILE OF THE REFERENCE MODEL

The correlation function is an important statistic in designing communication link that characterizes how fast a wireless channel changes with time, movement, or in frequency. For example, if the correlation stays high for a long time, in a case of strong channel attenuation, multiple symbols will be similarly affected implying that error correction codes will not be able to repair damage. These statistics enable the system designer to make informed decisions when choosing modulation, interleaving, and coding schemes at the transmitting end and the type of channel estimator and decoder at the receiving end. The specific correlation function that is of interest in this paper is the frequency correlation function (FCF), which measures the channels frequency selectivity. In other words, FCF is a useful indicator of dependencies as a function of difference in frequency ( $\Delta f$ ), and they can be used to access the required frequency difference between sample points for the values to be effectively uncorrelated.

The normalized frequency auto-correlation function of the time-invariant transfer function is defined as

$$R(\Delta f) = \frac{E[T(f)^*T(f + \Delta f)]}{\sqrt{\text{Var}[T(f)^*]\text{Var}[T(f + \Delta f)]}}, \quad (11)$$

where  $(\cdot)^*$  denotes complex conjugate operation,  $E[\cdot]$  is the statistical expectation operator, and  $\text{Var}[\cdot]$  is the statistical variance operator.

Since  $T^{SB}(f)$ , and  $T^{DB}(f)$  are independent zero-mean complex Gaussian random processes, (11) can be simplified to

$$R(\Delta f) = R^{SB}(\Delta f) + R^{DB}(\Delta f) + R^{LoS}(\Delta f), \quad (12)$$

where  $R^{SB}(\Delta f)$ ,  $R^{DB}(\Delta f)$ , and  $R^{LoS}(\Delta f)$  denote the normalized FCF's of the SB, DB, and LoS components, respectively, and are defined as

$$R^{SB}(\Delta f) = \frac{E[T^{SB}(f)^*T^{SB}(f + \Delta f)]}{\Omega}, \quad (13)$$

$$R^{DB}(\Delta f) = \frac{E[T^{DB}(f)^*T^{DB}(f + \Delta f)]}{\Omega}, \quad (14)$$

$$R^{LoS}(\Delta f) = \frac{E[T^{LoS}(f)^*T^{LoS}(f + \Delta f)]}{\Omega}, \quad (15)$$

where  $\Omega = D^{-\gamma/2}\sqrt{G_T G_R \lambda}/4\pi$ .

Since the number of local scatterers in the reference model described in Section II is infinite, the discrete AoDs  $\alpha_T^{(l,m)}$ , AoAs  $\alpha_R^{(p,q)}$ , and radii  $R_t^{(l)}$  and  $R_r^{(p)}$  can be replaced with continuous random variables  $\alpha_T$ ,  $\alpha_R$ ,  $R_t$ , and  $R_r$  with probability density functions (pdf)  $f(\alpha_T)$ ,  $f(\alpha_R)$ ,  $f(R_t)$ , and  $f(R_r)$ , respectively.

Substituting (42) into (15), the  $R^{LoS}(\Delta f)$  becomes

$$R^{LoS}(\Delta f) = \frac{K}{K+1} e^{-j\frac{2\pi}{c_0}\Delta f D}. \quad (16)$$

Similarly, substituting (40) into (13), and (41) into (14), the  $R^{SB}(\Delta f)$  and  $R^{DB}(\Delta f)$  can be written as (17) and (18) (appearing on page 5), respectively. Note that the FCFs for the SB and DB components of the time-invariant transfer function must be evaluated numerically because the integrals in (17)

and (18) do not have closed-form solutions. While it is difficult to obtain closed-form solutions, we show in Appendix C how the  $R^{SB}(\Delta f)$  and the  $R^{DB}(\Delta f)$  expressions can be approximated by

$$\begin{aligned} R^{SR}(\Delta f) &\approx \frac{2}{(\alpha_{T2} - \alpha_{T1})(R_{t2}^2 - R_{t1}^2)} \frac{\eta_{SR}}{K+1} \\ &\times \int_{R_{t1}}^{R_{t2}} R_t e^{-j\frac{2\pi}{c_0}\Delta f(R_t+D)} \int_{\alpha_{T1}}^{\alpha_{T2}} \frac{1}{1 + \gamma\frac{R_t}{D}(1 - \cos \alpha_T)} \\ &\times e^{-j\frac{2\pi}{c_0}\Delta f R_t \cos \alpha_T} d\alpha_T dR_t, \quad (19) \\ R^{DR}(\Delta f) &\approx \frac{2}{(\alpha_{R2} - \alpha_{R1})(R_{r2}^2 - R_{r1}^2)} \\ &\times \frac{\eta_{DR}}{K+1} \\ &\times \int_{R_{r1}}^{R_{r2}} R_r e^{-j\frac{2\pi}{c_0}\Delta f R_r} \int_{\alpha_{R1}}^{\alpha_{R2}} e^{-j\frac{2\pi}{c_0}\Delta f R_r \cos \alpha_R} \\ &\times \int_{R_{t1}}^{R_{t2}} R_t e^{-j\frac{2\pi}{c_0}\Delta f R_t} \\ &\times \int_{\alpha_{T1}}^{\alpha_{T2}} \frac{e^{j\frac{2\pi}{c_0}\Delta f(R_t \cos \alpha_T)}}{1 + \gamma\left(\frac{R_t}{D}(1 - \cos \alpha_T) + \frac{R_r}{D}(1 + \cos \alpha_R)\right)} \\ &\times d\alpha_T dR_t d\alpha_R dR_r, \quad (20) \end{aligned}$$

respectively.

To validate assumptions used to obtain the approximated FCFs in (19) and (20), we compare these equations with the numerically obtained FCFs correlations in (17) and (18). Figures 2 and 3 compare the exact and approximated frequency correlation functions for SR and DR components. Two different scatterer positions defined by the parameters,  $R_{t1}$ ,  $R_{t2}$ ,  $R_{r1}$ ,  $R_{r2}$ , and  $\theta_T$  (or  $\theta_R$ ) have been selected: the scenario,  $R_{t1} = R_{r1} = 0$  m,  $R_{t2} = R_{r2} = 0.11$  m, and  $\theta_T = \theta_R = 45^\circ$ , is shown in Fig. 2; and the scenario  $R_{t1} = R_{r1} = 0.2$  m,  $R_{t2} = R_{r2} = 0.3$  m, and  $\theta_T = \theta_R = 30^\circ$  is shown in Fig. 3. The T-R separation distance,  $D$ , is set to 0.3 m for both scenarios.

The mismatch between exact and approximated frequency correlation functions observed in Fig. 2 and 3 comes from the discrepancy between the exact (Eq. (6), (7)) and approximated (Eq. (43), (44)) expressions for the path lengths, i.e.,  $\epsilon_R^{(l,m)}$  and  $\epsilon_S^{(l,m,p,q)}$  (please refer to Appendix C). Specifically, for SR rays, the criterion that can approximate (6) with (43) is

$$\frac{R_t \sin \alpha_T}{D - R_t \cos \alpha_T} \ll 1 \quad (21)$$

Therefore, the accuracy of the approximation, for SR rays, depends on the degree to which the condition (21) is true. For Fig. 2, the maximum value of  $\frac{R_t \sin \alpha_T}{D - R_t \cos \alpha_T}$  is 0.35. While it is smaller than 1, the value is still not small enough to satisfy (21), which is why there exists mismatch between the exact and approximated correlation functions in Fig. 2. On the other hand, in the case of Fig. 3, the maximum value of  $\frac{R_t \sin \alpha_T}{D - R_t \cos \alpha_T}$  is 3.7321, which does not satisfy the condition at all. As a result, we can observe that the approximated correlation function for SR component has completely different shape

$$\begin{aligned}
R^{SB}(\Delta f) &= \mathbb{E} \left[ \frac{\eta_{SR}}{K+1} \frac{D^\gamma e^{-j2\pi\Delta f\tau_{SR}}}{\left( R_t + \frac{R_t \cos \alpha_T - D}{\cos \left[ \tan^{-1} \left( -\frac{R_t \sin \alpha_T}{D - R_t \cos \alpha_T} \right) + \pi \right]} \right)^\gamma} \right] \\
&= \frac{\eta_{SR}}{K+1} \int_{R_{t1}}^{R_{t2}} \int_{\alpha_{T1}}^{\alpha_{T2}} \frac{D^\gamma}{\left( R_t + \frac{R_t \cos \alpha_T - D}{\cos \left[ \tan^{-1} \left( -\frac{R_t \sin \alpha_T}{D - R_t \cos \alpha_T} \right) + \pi \right]} \right)^\gamma} e^{-j2\pi\Delta f\tau_{SR}} f(R_t) f(\alpha_T) d\alpha_T dR_t \\
&= \frac{2D^\gamma}{(\alpha_{T2} - \alpha_{T1})(R_{t2}^2 - R_{t1}^2)} \frac{\eta_{SR}}{K+1} \int_{R_{t1}}^{R_{t2}} \int_{\alpha_{T1}}^{\alpha_{T2}} \frac{R_t}{\left( R_t + \frac{R_t \cos \alpha_T - D}{\cos \left[ \tan^{-1} \left( -\frac{R_t \sin \alpha_T}{D - R_t \cos \alpha_T} \right) + \pi \right]} \right)^\gamma} \\
&\quad \times e^{-j\frac{2\pi}{c_0}\Delta f \left( R_t + \frac{R_t \cos \alpha_T - D}{\cos \left[ \tan^{-1} \left( -\frac{R_t \sin \alpha_T}{D - R_t \cos \alpha_T} \right) + \pi \right]} \right)} d\alpha_T dR_t, \tag{17}
\end{aligned}$$

$$\begin{aligned}
R^{DB}(\Delta f) &= \frac{\eta_{DR}}{K+1} \int_{R_{r1}}^{R_{r2}} \int_{R_{t1}}^{R_{t2}} \int_{\alpha_{R1}}^{\alpha_{R2}} \int_{\alpha_{T1}}^{\alpha_{T2}} \frac{D^\gamma e^{-j2\pi\Delta f\tau_{DR}} f(R_t, \alpha_T, R_r, \alpha_R)}{\left( R_t + R_r + \sqrt{|R_t \sin \alpha_T - R_r \sin \alpha_R|^2 + |R_t \cos \alpha_T - R_r \cos \alpha_R - D|^2} \right)^\gamma} d\alpha_T d\alpha_R dR_t dR_r \\
&= \frac{4D^\gamma}{(\alpha_{T2} - \alpha_{T1})(\alpha_{R2} - \alpha_{R1})(R_{t2}^2 - R_{t1}^2)(R_{r2}^2 - R_{r1}^2)} \frac{\eta_{DR}}{K+1} \int_{R_{r1}}^{R_{r2}} \int_{R_{t1}}^{R_{t2}} \int_{\alpha_{R1}}^{\alpha_{R2}} \int_{\alpha_{T1}}^{\alpha_{T2}} \frac{R_t R_r}{\left( R_t + R_r + \sqrt{|R_t \sin \alpha_T - R_r \sin \alpha_R|^2 + |R_t \cos \alpha_T - R_r \cos \alpha_R - D|^2} \right)^\gamma} \\
&\quad \times e^{-j\frac{2\pi}{c_0}\Delta f \left( R_t + R_r + \sqrt{|R_t \sin \alpha_T - R_r \sin \alpha_R|^2 + |R_t \cos \alpha_T - R_r \cos \alpha_R - D|^2} \right)} d\alpha_T d\alpha_R dR_t dR_r. \tag{18}
\end{aligned}$$

compared to the exact one in Fig. 3. Meanwhile, for DR rays, the assumption that approximates (7) with (44) is

$$|R_t^{(l)} \sin \alpha_T^{(l,m)} - R_r^{(p)} \sin \alpha_R^{(p,q)}|^2 = 0, \tag{22}$$

such that the first term of (7), which is the projection of  $\epsilon_s^{(l,m,p,q)}$  onto y-axis, cancels out. In Fig. 2, the geometry of the scenario described by the parameters,  $R_{t1} = R_{r1} = 0$  m,  $R_{t2} = R_{r2} = 0.1$  m, and  $\theta = 45^\circ$ , allows for a margin of error since there exists a chance that  $|R_t^{(l)} \sin \alpha_T^{(l,m)} - R_r^{(p)} \sin \alpha_R^{(p,q)}|^2 > 0$  due to large beamwidth ( $\theta = 45^\circ$ ). This explains the slight mismatch between the exact and approximated correlation functions for DR component in Fig. 2. On the other hand, in Fig. 3, where the parameters are  $R_{t1} = R_{r1} = 0.2$  m,  $R_{t2} = R_{r2} = 0.3$  m, and  $\theta = 30^\circ$ , smaller beamwidth forces the y-projections of  $\epsilon_s^{(l,m,p,q)}$  closer to 0. Therefore, the degree to which (22) is true is much higher in this case, and consequently, much better match between the exact and approximated correlation functions is observed for DR component in Fig. 3, compared to that in Fig. 2. Note that the benefit of the approximated expressions for correlation functions is a quick estimate of channel's frequency selectivity, and the exact correlation functions can be numerically obtained if more precise results are needed.

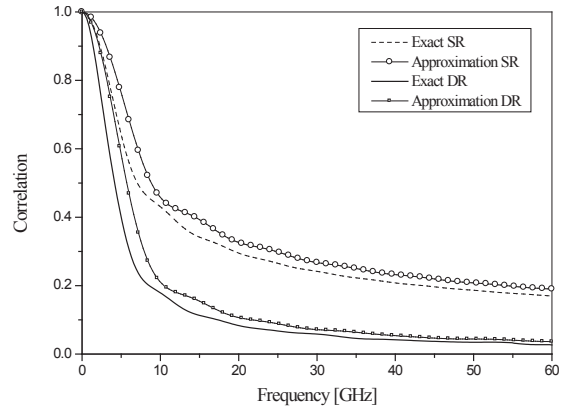


Fig. 2. The exact and approximated frequency correlation functions for SR and DR components when  $R_{t1} = R_{r1} = 0$  m,  $R_{t2} = R_{r2} = 0.11$  m,  $\theta_T = \theta_R = 45^\circ$ .

The power delay profile (PDP) of the proposed model can be obtained by taking the Inverse Fourier Transform of the FCF [33], i.e.,

$$P(\tau) = \mathcal{F}_{\Delta f}^{-1}\{R(\Delta f)\}. \tag{23}$$

The significance of PDP is that it gives the intensity of a received signal as a function of time delay, and is useful in

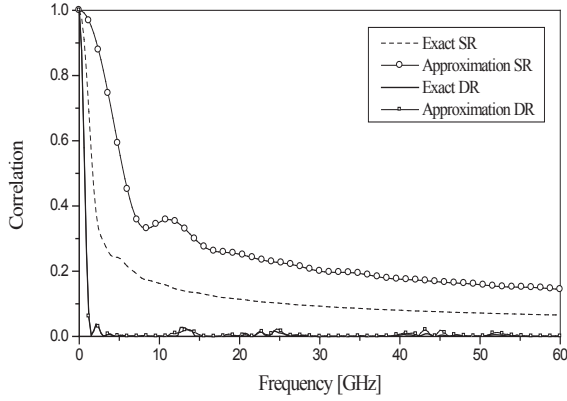


Fig. 3. The exact and approximated frequency correlation functions for SR and DR components when  $R_{t1} = R_{r1} = 0.2$  m,  $R_{t2} = R_{r2} = 0.3$  m,  $\theta_T = \theta_R = 30^\circ$ .

identifying multipaths in the channel. Also, PDPs are used to extract important parameters, such as RMS delay spread (and coherence bandwidth of the channel), which is a measure of time dispersion or frequency selectivity, and tell system designer how long it has to wait before next symbol can be sent to avoid inter-symbol interference.

To verify the validity of the proposed model, the theoretical PDP's are compared to the measured ones. The measurement data has been collected at two sub-THz frequency ranges, i.e., at  $f_c = 300$  GHz with 20 GHz of bandwidth [6], [8] and at D-band (110 – 170 GHz) [7]. Specifically, measurements at 300 GHz are analyzed for LoS desktop scenarios [6], realistic desktop environment with objects, such as books, cell phones, and laptops, and computer motherboard environment with a RAM module. Also, in D-band, measurements for NLoS desktop scenario with cylindrical obstruction [7] are used to validate the proposed model.

For 300 GHz desktop LoS measurement campaign [6], the two T-R separation distances,  $D$ , of 30 cm and 40 cm have been considered, and the  $T_x$  and  $R_x$  were equipped with horn antennas with beamwidths of  $10^\circ$ , i.e.,  $2\theta_T = 2\theta_R = 10^\circ$ . The  $T_x$  and  $R_x$ , as well as any surrounding objects, were stationary, meaning the channel was quasi-static with no time-dependence. Although the channel environment was free of local scatterers, the metallic surfaces of the  $T_x$  and  $R_x$  test heads, on which the horn antennas are attached, acted as reflectors. Consequently, the signal transmitted from  $T_x$  traveled the separation distance,  $D$ , got reflected off the  $R_x$  test head, traveled back the distance,  $D$ , towards  $T_x$ , reflected again off  $T_x$  test head this time, and finally, arrived at  $R_x$  after traversing the distance,  $D$ . This implies that, even though no scatterers were present in the environment, the multiple rays have been reflected off metallic transceiver box and created multiple scattering rays in the channel, introducing double-reflected rays in addition to the direct LoS ray. The arrivals of these double-reflected paths are apparent in the measured PDP's shown in Figs. 4(a) and 4(b). The excess delays of the double-reflected rays correspond to the rays that traveled double the separation distance, which is why the peaks in PDPs shift to the right as the distance increases.

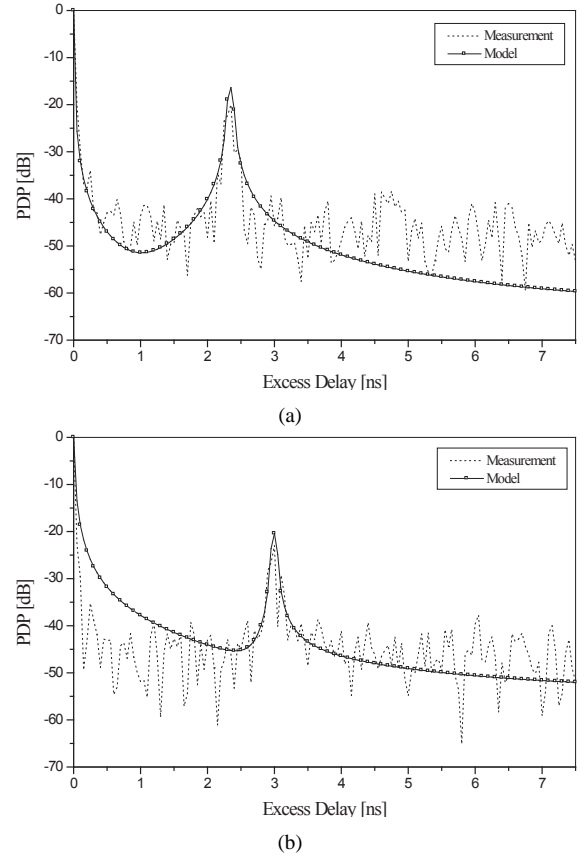


Fig. 4. The normalized theoretical and measured power delay profiles for the 300 GHz desktop LoS scenarios: (a)  $D = 30$  cm (b)  $D = 40$  cm.

In the reference model, parameter  $K$  is estimated using method in [34] to be 0.4 for all distances. Since there are no single reflections in the channel, setting the parameters  $\eta_{SR}$  and  $\eta_{DR}$  was straight forward, i.e.  $\eta_{SR} = 0$  and  $\eta_{DR} = 1$ . The parameters  $R_{t1}$ ,  $R_{r1}$ ,  $R_{t2}$ , and  $R_{r2}$  are estimated using method in [31] as:  $R_{t1} = R_{r1} = 32$  cm and  $R_{t2} = R_{r2} = 33$  cm for  $D = 30$  cm (Fig. 4(a)), and  $R_{t1} = R_{r1} = 42$  cm and  $R_{t2} = R_{r2} = 43$  cm for  $D = 40$  cm (Fig. 4(b)), respectively.

Figures 4(a) and 4(b) show that the proposed model captures well the amplitudes and the excess delays of the LoS and double-reflected multipath components for the two distances. Measurements indicate that the signal power drops to a negligible level after bouncing off the test head surfaces multiple times. Hence, it is sufficient for the reference model to include only the single and double-reflected multipath components. Note that a mismatch between the modeled and measured PDP's is observed towards larger excess delays because the measurement has reached its noise floor, while the model does not take into account the noise threshold of the receiver.

In addition to LoS desktop scenario, we also compare our measured and modeled PDPs in a more realistic device-to-device communication scenario shown in Fig. 5(a), where different objects, such as a book, a phone, a stack of paper, and a laptop, are placed on a desk to obstruct the LoS between the  $T_x$  and the  $R_x$ . Figure 5(b) presents the modeled and measured PDP's for the measurement setup of Fig. 5(a). The T-R separation,  $D$ , is 55 cm, and other parameters are estimated

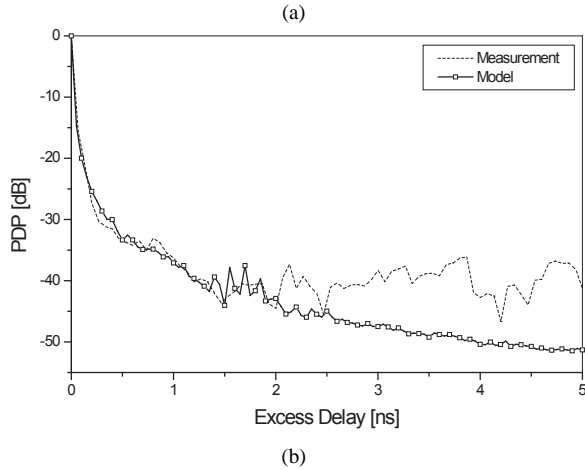


Fig. 5. Realistic 300 GHz device-to-device desktop scenario with clutter: (a) Measurement setup and (b) Comparison of measured and modeled PDP's.

using the methods from [34] and [31] as follows:  $K = 0.5$ ,  $\eta_{SR} = 0.3$ , and  $\eta_{DR} = 0.7$ ,  $R_{t1} = R_{r1} = 10$  cm, and  $R_{t2} = R_{r2} = 50$  cm. The random variables,  $R_t$ ,  $R_r$ ,  $\alpha_T$ , and  $\alpha_R$ , are assumed to be uniformly distributed with the joint pdf of (9), and it has been proven that this assumption is valid for the realistic desktop propagation environment with cluttered scatterers by observing a good match between the theoretical and measured PDP's in Fig. 5(b).

Another potential THz application is chip-chip communication, where ultra-wideband channels over short distances are required. To illustrate validity of our model, we compare our modeled PDP with the measured one for a NLoS scenario in computer motherboard environment, where a RAM module (DIMM) is placed perpendicularly at the midpoint of the T-R separation distance, 23.5 cm, blocking the LoS. The measurement setup and the PDP's are presented in Fig. 6(a) and 6(b), respectively. The measured PDP shown in Fig. 6(b) shows two distinct paths reaching the  $R_x$ , i.e., at  $\tau = 0$  ns  $\tau = 0.93$  ns. From the fact that the backside of the DIMM is metallic, it can be concluded that the first arriving path at  $\tau = 0$  ns is the path that diffracts off the top edge of the RAM (i.e. single-reflected ray). On the other hand, considering the geometry of the setup and the excess delay of 0.93 ns of the second arriving path, it is reasonable to assume that the second path is the result of two consecutive reflections off the  $R_x$  back panel and the back side of the DIMM (i.e. double-reflected rays). The modeled PDP in Fig. 6(b), which accurately predicts the excess delay and amplitude of the second arriving path, is

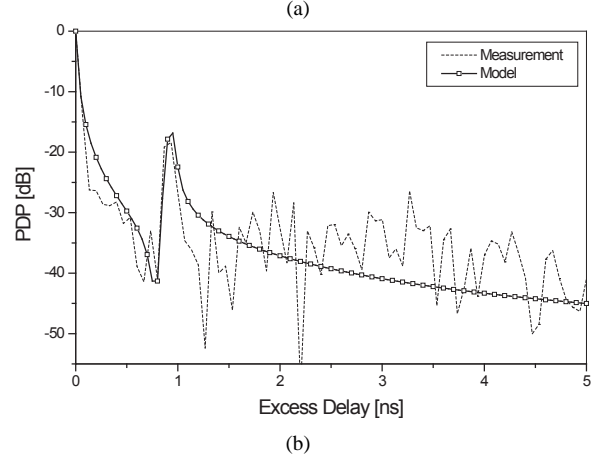
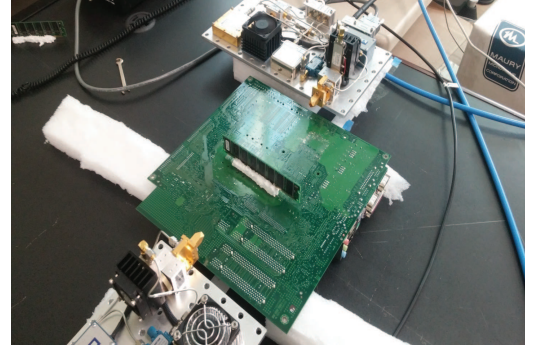


Fig. 6. 300 GHz NLoS scenario in computer motherboard environment with a RAM module (DIMM) as obstruction: (a) Measurement setup and (b) Comparison of measured and modeled PDP's.

produced with the following parameters:  $K = 0$ ,  $\eta_{SR} = 0.45$ ,  $\eta_{DR} = 0.55$ ,  $D = 23.5$  cm,  $R_{t1} = 25.5$  cm,  $R_{t2} = 26.5$  cm,  $R_{r1} = 11$  cm, and  $R_{r2} = 12$  cm. As before, the estimation of  $K$  is based on the method from [34], while that of other parameters are estimated using the method in [31]. The Rician factor,  $K$ , of 0 agrees with intuition since there is no LoS path in this scenario, and the estimated contribution factors,  $\eta_{SR}$ ,  $\eta_{DR}$ , reveal that the DR rays have slightly higher contribution to the total received power than the SR rays.

Finally, we compare measured and modeled PDPs in a NLoS scenario, where a cylindrical object, such as a coffee mug, obstructs the line of sight. The measurements are collected in D-band [7] with a coffee mug obstructing the LoS between the  $T_x$  and the  $R_x$ . The mug is placed at the midpoint of the T-R separation distance, i.e.,  $D = 35.56$  cm. The measurement setup is shown in Fig. 7(a). In [7], for this particular scenario, we have shown that the received power is a vector sum of LoS, convex-surface-diffracted rays (i.e., single-reflected rays), and the double-reflected rays (i.e., reflections inside the mug). For this scenario, the model parameters are estimated as follows:  $K = 0.15$ ,  $\eta_{SR} = \eta_{DR} = 0.5$ ,  $R_{t1} = R_{r1} = 21.5$  cm, and  $R_{t2} = R_{r2} = 22.5$  cm, using the methods from [34] and [31], respectively.

#### IV. SIMULATION MODEL FOR SHORT-RANGE WIDEBAND SUB-THZ CHANNELS

The reference model for short-range wideband sub-THz channels described in Section II assumes an infinite number

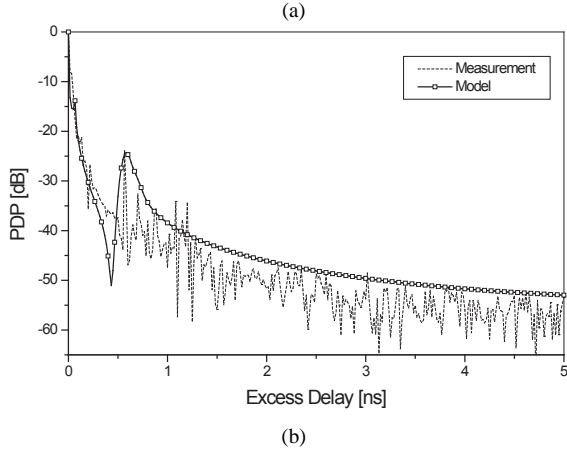
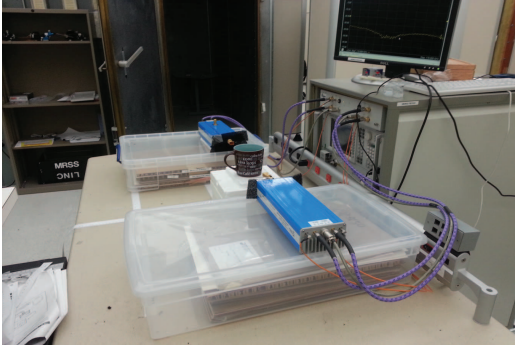


Fig. 7. D-band desktop NLoS scenario with cylindrical obstruction: (a) Measurement setup and (b) Comparison of measured and modeled PDP's.

of scatterers, which prevents practical implementation. It is desirable to design simulation model with a finite (preferably small) number of scatterers, while still matching the statistical properties of the reference model.

The simulation model proposed in this paper uses the statistical Sum-of-Sinusoids (SoS) method, which generates the channel waveform by superimposing a finite number of properly selected sinusoids [33], i.e., LoS, Single-Reflected (SR), and Double-Reflected (DR) components. Also, in this statistical SoS model, the parameter sets,  $(R_t, R_r)$  and  $(\alpha_T, \alpha_R)$ , are left as random variables that vary with each simulation trial. Therefore, the statistical properties of the SoS model vary for each trial, but converge to the desired properties when averaged over a sufficient number of simulations.

Using the reference model in (1) with a finite number of scatterers and assuming 2-D isotropic scattering, the following function is considered for the received complex faded envelope

$$\begin{aligned}
 h(\tau) = & \sqrt{\frac{\eta_{SR}}{K+1}} \frac{1}{\sqrt{M}} \sum_{l=1}^L \sum_{m=1}^{M^{(l)}} A_{l,m} e^{j\phi_{l,m}} \delta(\tau - \tau_{l,m}) \\
 & + \sqrt{\frac{\eta_{DR}}{K+1}} \frac{1}{\sqrt{MQ}} \sum_{l,m=1}^{L, M^{(l)}} \sum_{p,q=1}^{P, Q^{(p)}} A_{l,m,p,q} e^{j\phi_{l,m,p,q}} \delta(\tau - \tau_{l,m,p,q}) \\
 & + \sqrt{\frac{K}{K+1}} A_{LoS} e^{j\phi_{LoS}} \delta(\tau - \tau_{LoS}), \quad (24)
 \end{aligned}$$

where amplitudes and delays of SB, DB, and LoS components are defined in [7]. It is assumed that the angles of departure

$(\alpha_T^{(l,m)})$  and the angles of arrival  $(\alpha_R^{(p,q)})$  are uniformly distributed random variables. They are realized as follows:

$$\alpha_T^{(l,m)} = \frac{(m + \psi_T - 1)(\alpha_{T2} - \alpha_{T1})}{M} + \alpha_{T1}, \quad (25)$$

$$\alpha_R^{(p,q)} = \frac{(q + \psi_R - 1)(\alpha_{R2} - \alpha_{R1})}{Q} + \alpha_{R1}, \quad (26)$$

for  $l = 1, \dots, L$ ,  $m = 1, \dots, M$ ,  $p = 1, \dots, P$ , and  $q = 1, \dots, Q$ . Furthermore, it is assumed that the radii  $R_t^{(l)}$  and  $R_r^{(p)}$  are uniformly distributed independent random variables implemented as follows:

$$R_t^{(l)} = \sqrt{\frac{(l + \sigma_T - 1)(R_{t2}^2 - R_{t1}^2)}{L} + R_{t1}^2}, \quad (27)$$

$$R_r^{(p)} = \sqrt{\frac{(p + \sigma_R - 1)(R_{r2}^2 - R_{r1}^2)}{P} + R_{r1}^2}, \quad (28)$$

for  $l = 1, \dots, L$ ,  $m = 1, \dots, M$ ,  $p = 1, \dots, P$ , and  $q = 1, \dots, Q$ . Finally, it is assumed that the phases  $\phi_{l,m}$ ,  $\phi_{p,q}$ , and  $\phi_{l,m,p,q}$  are uniform random variables on the interval  $[-\pi, \pi)$  that are independent from the angles of departure, the angles of arrival, and the radii of the sectors. The parameters,  $\sigma_T$ ,  $\sigma_R$ ,  $\psi_T$ , and  $\psi_R$ , are independent random variables uniformly distributed on the interval  $[0,1)$ , such that 2-D isotropic scattering environment is ensured.

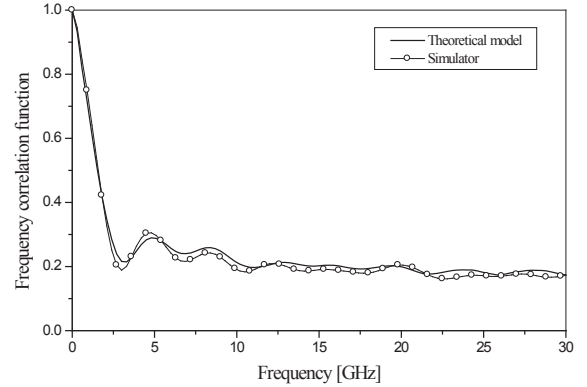


Fig. 8. The theoretical and simulated frequency correlation functions for  $R_{t1} = R_{r1} = 0.16$  m,  $R_{t2} = R_{r2} = 0.161$  m,  $\theta_T = \theta_R = 45^\circ$ ,  $K = 0.1$ ,  $\eta_{SR} = 0.5$ ,  $\eta_{DR} = 0.5$ , and  $L = M = P = Q = 4$

Figure 8 shows good agreement between the analytical and simulated correlation functions for the scenario modeled with the following parameters:  $R_{t1} = R_{r1} = 0.16$  m,  $R_{t2} = R_{r2} = 0.161$  m,  $D = 0.3$  m,  $\theta_T = \theta_R = 45^\circ$ ,  $K = 0.1$ ,  $\eta_{SR} = 0.5$ , and  $\eta_{DR} = 0.5$ . The number of scatterers was  $L = M = P = Q = 4$  and the correlation functions are averaged over  $N_{stat} = 400$  simulation trials. Corresponding PDP's are compared in Fig. 9. The results show that the theoretical and simulated FCF's and PDP's have a good match over a wide range of time delays.

Finally, Fig. 10 presents the theoretical, measured, and simulated PDP's on the same plot for the realistic 300 GHz desktop scenario shown in Fig. 5(a). For simulation, the same parameters that have been estimated for the theoretical PDP are used, and the number of scatterers is set by the parameters,  $L = M = P = Q = 6$ . All three PDP's are in a good

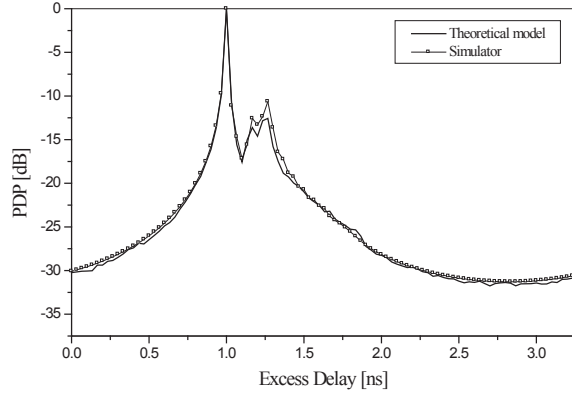


Fig. 9. The theoretical and simulated power delay profiles for  $R_{t1} = R_{r1} = 0.16$  m,  $R_{t2} = R_{r2} = 0.161$  m,  $\theta_T = \theta_R = 45^\circ$ ,  $K = 0.1$ ,  $\eta_{SR} = 0.5$ ,  $\eta_{DR} = 0.5$ , and  $L = M = P = Q = 4$

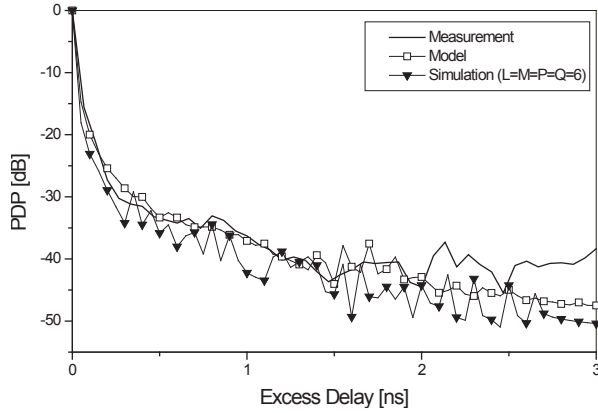


Fig. 10. The measured, modeled, and simulated PDPs for the realistic 300-GHz desktop scenario shown in Fig. 5(a).

agreement, which confirms the validity of the reference model as well as the simulation model.

## V. CONCLUSIONS

This paper proposed the two-dimensional (2-D) geometrical propagation model for short-range sub-THz device-to-device communications. Based on the geometrical model, a parametric reference model for wideband sub-THz multipath fading channels is developed. From the reference model, the corresponding FCF and PDP are derived and compared with measured data. The results show good agreement between the measured and theoretical PDP's. Finally, a new sum-of-sinusoids based simulation model for wideband sub-THz channels is proposed. The statistics of the reference model are verified by simulation. The results show that the simulation model is a good approximation of the reference model.

## APPENDIX A

### DERIVATIONS OF THE SINGLE-REFLECTED AND DOUBLE-REFLECTED PATH LENGTHS

In this section, we show the derivations for the expressions in (6) and (7). We start with the derivations for (6). From the triangle,  $A_T - S^{(l,m)} - A_R$ , in Fig. 1, we can observe that

$$\epsilon_T^{(l,m)} \cos \alpha_T^{(l,m)} + \epsilon_R^{(l,m)} \cos(\pi - \alpha_R^{(l,m)}) = D, \quad (29)$$

Hence, the distance  $\epsilon_R^{(l,m)}$  can be written as

$$\epsilon_R^{(l,m)} = \frac{\epsilon_T^{(l,m)} \cos \alpha_T^{(l,m)} - D}{\cos \alpha_R^{(l,m)}}. \quad (30)$$

Now,  $\alpha_R^{(l,m)}$  can also be expressed in terms of  $\epsilon_T^{(l,m)}$  and  $\alpha_T^{(l,m)}$  using the sine rule:

$$\frac{\epsilon_T^{(l,m)}}{\sin(\pi - \alpha_R^{(l,m)})} = \frac{D}{\sin(\alpha_R^{(l,m)} - \alpha_T^{(l,m)})}. \quad (31)$$

Using (30) and (31),  $\epsilon_R^{(l,m)}$  can be written as

$$\epsilon_R^{(l,m)} = \frac{R_t^{(l)} \cos \alpha_T^{(l,m)} - D}{\cos \left[ \tan^{-1} \left( \frac{R_t^{(l)} \sin \alpha_T^{(l,m)}}{D - R_t^{(l)} \cos \alpha_T^{(l,m)}} \right) + \pi \right]}, \quad (32)$$

Now we show the derivations for (7). From Fig. 1, we can represent the length of  $\epsilon_S^{(l,m,p,q)}$  as a sum of the projections to x- and y-axis, i.e.,  $\epsilon_S^{(l,m,p,q)} = \sqrt{X^2 + Y^2}$ .

We can find X projection by solving the following equations:

$$X = D - (Z + W) \quad (33)$$

$$X + Z = \epsilon_T^{(l,m)} \cos \alpha_T^{(l,m)} \quad (34)$$

$$X + W = \epsilon_R^{(p,q)} \cos(\pi - \alpha_R^{(p,q)}), \quad (35)$$

where  $Z$  and  $W$  are, respectively, the distances  $A_T - S^{(p,q)}$  and  $A_R - S^{(l,m)}$  projected onto the x-axis. Adding (34) and (35), we get

$$2X + Z + W = \epsilon_T^{(l,m)} \cos \alpha_T^{(l,m)} - \epsilon_R^{(p,q)} \cos \alpha_R^{(p,q)}. \quad (36)$$

Then, substituting (33) into (36),  $X$  can be written as:

$$X = \left| \epsilon_T^{(l,m)} \cos \alpha_T^{(l,m)} - \epsilon_R^{(p,q)} \cos \alpha_R^{(p,q)} - D \right|. \quad (37)$$

Using similar reasoning,  $Y$  component can be written as:

$$Y = \left| \epsilon_T^{(l,m)} \sin \alpha_T^{(l,m)} - \epsilon_R^{(p,q)} \sin \alpha_R^{(p,q)} \right|. \quad (38)$$

Then, the final expression for  $\epsilon_S^{(l,m,p,q)}$  is

$$\epsilon_S^{(l,m,p,q)} = \left[ \left| \epsilon_T^{(l,m)} \sin \alpha_T^{(l,m)} - \epsilon_R^{(p,q)} \sin \alpha_R^{(p,q)} \right|^2 + \left| \epsilon_T^{(l,m)} \cos \alpha_T^{(l,m)} - \epsilon_R^{(p,q)} \cos \alpha_R^{(p,q)} - D \right|^2 \right]^{1/2}. \quad (39)$$

APPENDIX B  
THE SB, DB, AND LOS COMPONENTS OF THE  
TIME-INVARIANT TRANSFER FUNCTION

Using (1) - (8), the SB, DB, and LoS components of the time-invariant transfer function in (10) can be written as

$$T^{SB}(f) = \lim_{M \rightarrow \infty} \sqrt{\frac{\eta_{SR}}{K+1}} \frac{1}{\sqrt{M}} \sum_{l=1}^L \sum_{m=1}^{M^{(l)}} A_{SR}^{(l,m)} e^{-j2\pi f \tau_{SR}^{(l,m)} + j\phi_{SR}^{(l,m)}}, \quad (40)$$

$$T^{DB}(f) = \lim_{M,Q \rightarrow \infty} \sqrt{\frac{\eta_{DR}}{K+1}} \frac{1}{\sqrt{MQ}} \sum_{l,m=1}^{L,M^{(l)}} \sum_{p,q=1}^{P,Q^{(p)}} A_{DR}^{(l,m,p,q)} e^{-j2\pi f \tau_{DR}^{(l,m,p,q)} + j\phi_{DR}^{(l,m,p,q)}}, \quad (41)$$

$$T^{LoS}(f) = \sqrt{\frac{K}{K+1}} A_{LoS} e^{-j2\pi f \tau_{LoS} + j\phi_{LoS}}, \quad (42)$$

respectively, where the amplitudes,  $A_{SR}^{(l,m)}$ ,  $A_{DR}^{(l,m,p,q)}$ , and  $A_{LoS}$ , and the time delays,  $\tau_{SR}^{(l,m)}$ ,  $\tau_{DR}^{(l,m,p,q)}$ , and  $\tau_{LoS}$ , are defined in [7].

APPENDIX C  
THE APPROXIMATED FCF OF THE SB AND DB  
COMPONENTS

The expression in (17) can be further simplified by noting that distance in (6) can be approximated as

$$\epsilon_R^{(l,m)} \approx D - R_t^{(l)} \cos \alpha_T^{(l,m)} \quad (43)$$

under the assumption of Eq. (21). The expression in (43) is obtained using the trigonometric identity  $\cos(\tan^{-1} x) = 1/\sqrt{1+x^2}$ . Now applying the approximation  $(1+x)^n \approx 1+nx$  for small  $x$ , we obtain the expression for the approximated FCF of the SB component as in (19).

The expression in (18) can be further simplified by noting that distance in (7) can be approximated as

$$\epsilon_S^{(l,m,p,q)} \approx \left| R_t^{(l)} \cos \alpha_T^{(l,m)} - R_r^{(p)} \cos \alpha_R^{(p,q)} - D \right|. \quad (44)$$

Without loss of generality, we have assumed that  $R_t^{(l)} = R_r^{(p)}$  and  $\alpha_R^{(p,q)} = \pi - \alpha_T^{(l,m)}$ , which leads to the expression for the approximated FCF of the DB component as in (20).

REFERENCES

- [1] S. Cherry, "Edholm's law of bandwidth," *IEEE Spectrum*, vol. 41, pp. 58–60, July 2004.
- [2] P. H. Siegel, "Terahertz technology," *IEEE Transactions on Microwave Theory and Techniques*, MTT-50, pp. 910–928, March 2002.
- [3] S. Priebe, C. Jastrow, M. Jacob, T. Kleine-Ostmann, T. Schrader, T. Kürner, "Channel and propagation measurements at 300 GHz," *IEEE Transactions on Antennas and Propagation*, vol. 59, no. 5, pp. 1688–1698, May 2011.
- [4] R. Piesiewicz, T. Kleine-Ostmann, N. Krumbholz, D. Mittleman, M. Koch, J. Schoebel, and T. Kürner, "Short-range ultra-broadband terahertz communications: Concepts and perspectives," *IEEE Antennas and Propagation Magazine*, vol. 49, pp. 24–39, June 2007.
- [5] S. Kim and A. Zajic, "Path loss model for 300-GHz wireless channels," *Proc. of IEEE International Symposium on Antennas and Propagation*, pp. 1–2, Memphis, Tennessee, USA, July 2014.
- [6] S. Kim and A. Zajic, "Statistical characterization of 300-GHz propagation on a desktop," *IEEE Transactions on Vehicular Technology*, vol. 64, pp. 3330–3338, August 2015.

- [7] S. Kim, W.T. Khan, A. Zajic, and J. Papapolymerou, "D-Band Channel Measurements and Characterization for Indoor Applications," *IEEE Transactions on Antennas and Propagation*, vol. 63, pp. 3198–3207, July 2015.
- [8] S. Kim and A. Zajic, "300 GHz path loss measurements on computer motherboard," *10th European Conference on Antennas and Propagation*, Davos, Switzerland, April 2016.
- [9] Y. Yang, M. Mandehgar, and D. Grischkowsky, "Broadband THz pulse transmission through the atmosphere," *IEEE Transactions on Terahertz Science and Technology*, vol. 1, pp. 264–273, September 2011.
- [10] R. Piesiewicz, T. Kleine-Ostmann, N. Krumbholz, D. Mittleman, M. Koch, and T. Kürner, "Terahertz characterisation of building materials," *IEEE Electronic Letters*, vol. 41, pp. 1002–1004, 2005.
- [11] R. Piesiewicz, C. Jansen, D. Mittleman, T. Kleine-Ostmann, M. Koch, and T. Kürner, "Scattering analysis for the modeling of THz communication systems," *IEEE Transactions on Antennas and Propagation*, vol. 55, pp. 3002–3009, November 2007.
- [12] C. Jansen, R. Piesiewicz, D. Mittleman, T. Kürner, and M. Koch, "The impact of reflections from stratified building materials on the wave propagation in future indoor terahertz communication systems," *IEEE Transactions on Antennas and Propagation*, vol. 56, no. 5, pp. 1413–1419, 2008.
- [13] S. Priebe, M. Jacob, C. Jastrow, T. Kleine-Ostmann, T. Schrader, and T. Kürner, "A comparison of indoor channel measurements and ray tracing simulations at 300 GHz," *Proc. Int. Conf. Infrared Millim. Terahertz Waves (IRMMW-THz)*, 2010.
- [14] J. M. Jornet and I. F. Akyildiz, "Channel modeling and capacity analysis for electromagnetic wireless nanonetworks in the terahertz band," *IEEE Transactions on Wireless Communications*, vol. 10, pp. 3211–3221, October 2011.
- [15] H. Chong, A. Bicen, and I. F. Akyildiz, "Multi-ray channel modeling and wideband characterization for wireless communications in the terahertz band," *IEEE Transactions on Wireless Communications*, vol. 14, no. 5, pp. 2402–2412, May 2015.
- [16] M. Jacob, S. Priebe, R. Dickhoff, T. Kleine-Ostmann, T. Schrader, T. Kürner, "Diffraction in mm and sub-mm wave indoor propagation channels," *IEEE Transactions on Microwave Theory and Techniques*, vol. 60, no. 3, pp. 833–844, March 2012.
- [17] D. W. Matolak, S. Kaya, A. Kodi, "Channel modeling for wireless networks-on-chips," *IEEE Communications Magazine*, vol. 51, no. 6, pp. 180–186, June 2013.
- [18] S. Priebe and T. Kürner, "Stochastic modeling of THz indoor radio channels," *IEEE Transactions on Wireless Communications*, vol. 12, no. 9, pp. 4445–4455, September 2013.
- [19] A. F. Molisch, "Ultrawideband propagation channels-theory, measurement, and modeling," *IEEE Transactions on Vehicular Technology*, vol. 54, no. 5, pp. 1528–1545, September 2005.
- [20] A. A. M. Saleh and R. A. Valenzuela, "A statistical model for indoor multipath propagation," *IEEE Journal on Selected Areas in Communications*, vol. 5, no. 2, pp. 128–137, February 1987.
- [21] S. Kim and A. Zajic, "Statistical Modeling of THz Scatter Channels," *Proc. European Conf. Antennas and Propag. EUCap09*, pp. 1–5, Lisbon, Portugal, April 2015.
- [22] P. Smulders, "Exploiting the 60 GHz band for local wireless multimedia access: prospects and future directions," *IEEE Commun. Mag.*, vol. 40, no. 1, pp. 140–147, 2002.
- [23] M. Fryziel, C. Loyez, L. Clavier, N. Rolland, and P. A. Rolland, "Path-loss model of the 60-GHz indoor radio channel," *Microw. and Opt. Technology Lett.*, vol. 34, no. 3, pp. 158–162, 2002.
- [24] H. Xu, V. Kukshya, and T. S. Rappaport, "Spatial and temporal characteristics of 60-GHz indoor channels," *IEEE J. Sel. Areas Commun.*, vol. 20, no. 3, pp. 620–630, April 2002.
- [25] N. Moraitis and P. Constantinou, "Indoor channel measurements and characterization at 60 GHz for wireless local area network applications," *IEEE Transactions on Antennas and Propagation*, vol. 52, no. 12, pp. 3180–3189, December 2004.
- [26] T. Zwick, T. J. Beukema, and H. Nam, "Wideband channel sounder with measurements and model for the 60 GHz indoor radio channel," *IEEE Transactions on Vehicular Technology*, vol. 54, no. 4, pp. 1266–1276, July 2005.
- [27] H. Yang, P. F. M. Smulders, and M. H. A. J. Herben, "Indoor channel measurements and analysis in the frequency bands 2 GHz and 60 GHz," *Proc. IEEE Symp. Pers. Indoor Mob. Radio Commun.*, pp. 1–5, September 2005.
- [28] S. Geng, J. Kivinen, X. Zhao, and P. Vainikainen, "Millimeter-wave propagation channel characterization for short-range wireless commu-

nications,” *IEEE Transactions on Vehicular Technology*, vol. 58, no. 1, pp. 3–13, January 2009.

- [29] M. Peter and W. Keusgen, “Analysis and comparison of indoor wideband radio channels at 5 and 60 GHz,” *Proc. European Conf. Antennas and Propag. EUCap09*, pp. 3830–3834, March 2009.
- [30] T. S. Rappaport, S. Sun, R. Mayzus, H. Zhao, Y. Azar, K. Wang, G. N. Wong, J. K. Schulz, M. Samimi, F. Gutierrez, “Millimeter wave mobile communications for 5G Cellular: it will work!,” *Access, IEEE*, vol. 1, pp.335–349, May 2013.
- [31] A. G. Zajic, G. L. Stuber, T. G. Pratt, and S. Nguyen, “Wide-band MIMO mobile-to-mobile channels: statistical modeling with experimental verification”, *IEEE Transactions on Vehicular Technology*, vol. 58, pp. 517–534, February 2009.
- [32] A. G. Zajic and G. L. Stuber, “Space-time correlated MIMO mobile-to-mobile channels: modeling and simulation”, *IEEE Transactions on Vehicular Technology*, vol. 57, pp. 715-726, March 2008.
- [33] A. G. Zajić, *Mobile-to-Mobile Wireless Channels*. Artech House, Boston MA, January 2013.
- [34] L. J. Greenstein, D. G. Michelson, and V. Erceg, “Moment-method estimation of the Ricean K-factor,” *IEEE Commun. Letters*, vol. 3, pp. 175–176, June 1999.



**Seunghwan Kim** (S’14) Seunghwan Kim was born in Seoul, South Korea, in 1986. He received Bachelor of Applied Science in Electrical Engineering (with Distinction) from University of Waterloo, Canada, in 2009. During his degree, he has worked as a Research Assistant at the Telecommunication Group of Korea Electrotechnology Research Institute (KERI), and as a Hardware Engineer at Mitel Networks. He is currently pursuing the Ph.D. degree in Electrical Engineering at Georgia Institute of Technology in the area of channel measurement,

characterization, modeling, and antenna design for future THz device-to-device communication systems.



**Alenka Zajić** (S’99-M’09-SM’13) Alenka Zajić received the B.Sc. and M.Sc. degrees from the School of Electrical Engineering, University of Belgrade, in 2001 and 2003, respectively. She received her Ph.D. degree in Electrical and Computer Engineering from the Georgia Institute of Technology in 2008. Currently, she is an Assistant Professor in School of Electrical and Computer Engineering at Georgia Institute of Technology. Prior to that, she was visiting faculty in School of Computer Science at Georgia Institute of Technology, a post-doctoral

fellow in the Naval Research Laboratory, and design engineer at Skyworks Solutions Inc. Her research interests span areas of electromagnetics, wireless communications, signal processing, and computer engineering.

Dr. Zajić received the Neal Shepherd Memorial Best Propagation Paper Award, the Best Paper Award at ICT 2008, the Best Student Paper Award at WCNC 2007, and was also the recipient of the Dan Noble Fellowship in 2004, awarded by Motorola Inc. and IEEE Vehicular Technology Society for quality impact in the area of vehicular technology. Currently, she is an editor for IEEE Transactions on Wireless Communications and the Chair of the IEEE MTT/AP Atlanta Chapter.